WILEY-VCH

ADVANCED HEALTHCARE MATERIALS

Supporting Information

for *Adv. Healthcare Mater.*, DOI: 10.1002/adhm.202101077

Dual ultrasound and photoacoustic tracking of magnetically-driven micromotors: from in vitro to in vivo

*Azaam Aziz, Joost Holthof, Sandra Meyer, Oliver G. Schmidt and Mariana Medina-Sánchez**

Supporting Information

Dual ultrasound and photoacoustic tracking of magnetically-driven micromotors: from in vitro to in vivo

*Azaam Aziz, Joost Holthof, Sandra Meyer, Oliver G. Schmidt and Mariana Medina-Sánchez**

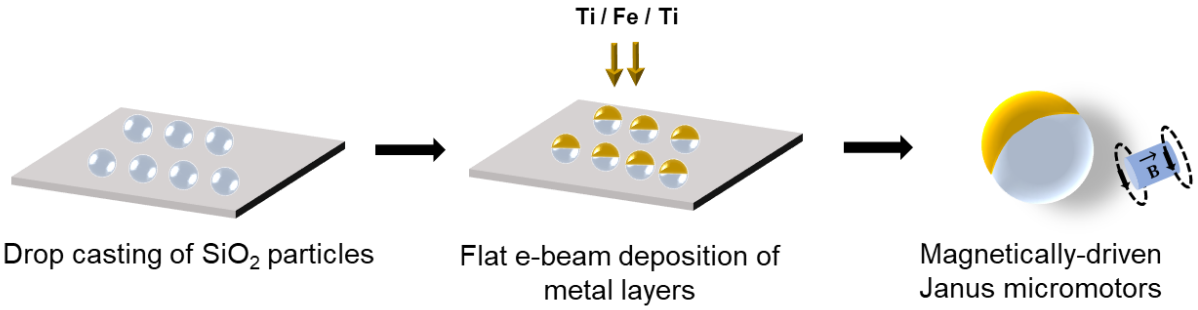

Figure S1. Fabrication of the magnetically-driven micromotors. A monolayer of SiO_2 particles (⌀ = 100 µm) is drop-casted on a glass slide and dried at room temperature. Afterward, thin metal layers (10 nm Ti, 50 nm Fe and 10 nm Ti) are deposited using an electron beam evaporator.

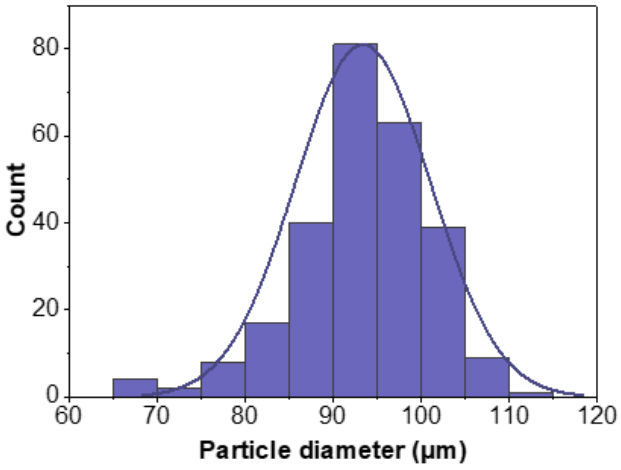

Figure S2. The particle size distribution histogram of SiO_2 microparticles with mean diameter of 93.30 µm (SD ± 7.70 µm).

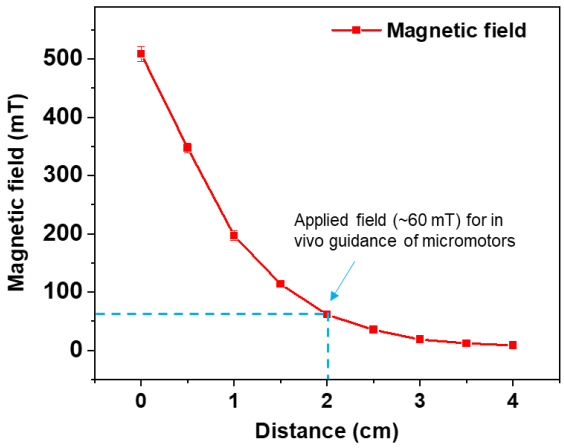

Figure S3. The magnetic field strength of an external hand-held magnet was measured using a Hall sensor from 0 to 4 cm distance.

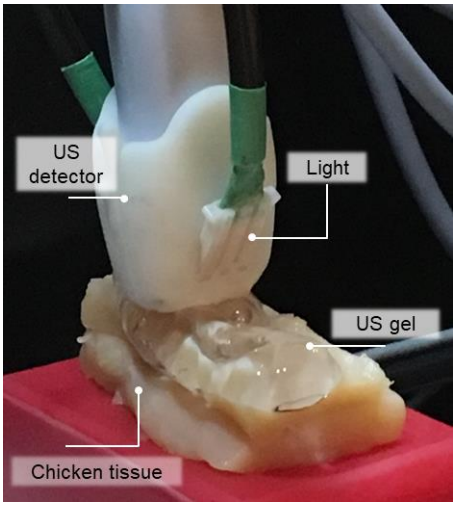

Figure S4. The micromotors are inserted in IPU tubing which is then sandwiched between two chicken breast tissues. The conventional US gel was applied between the acoustic transducer and the chicken surface for efficient acoustic coupling.

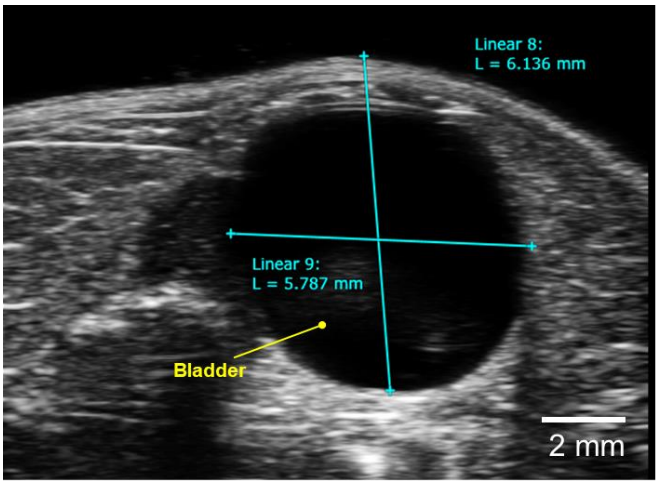

Figure S5. Dimensions of a bladder cavity of a 12-week-old mouse.

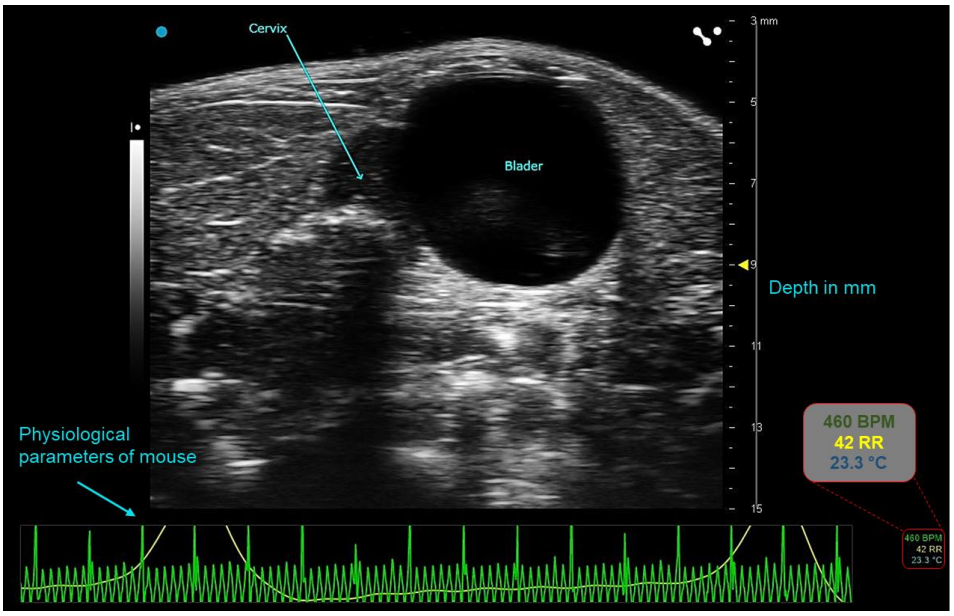

Figure S6. Physiological parameters of a mouse during the experiment. Beats per minute (BPM) (heart rate) and Respiratory rate (RR).

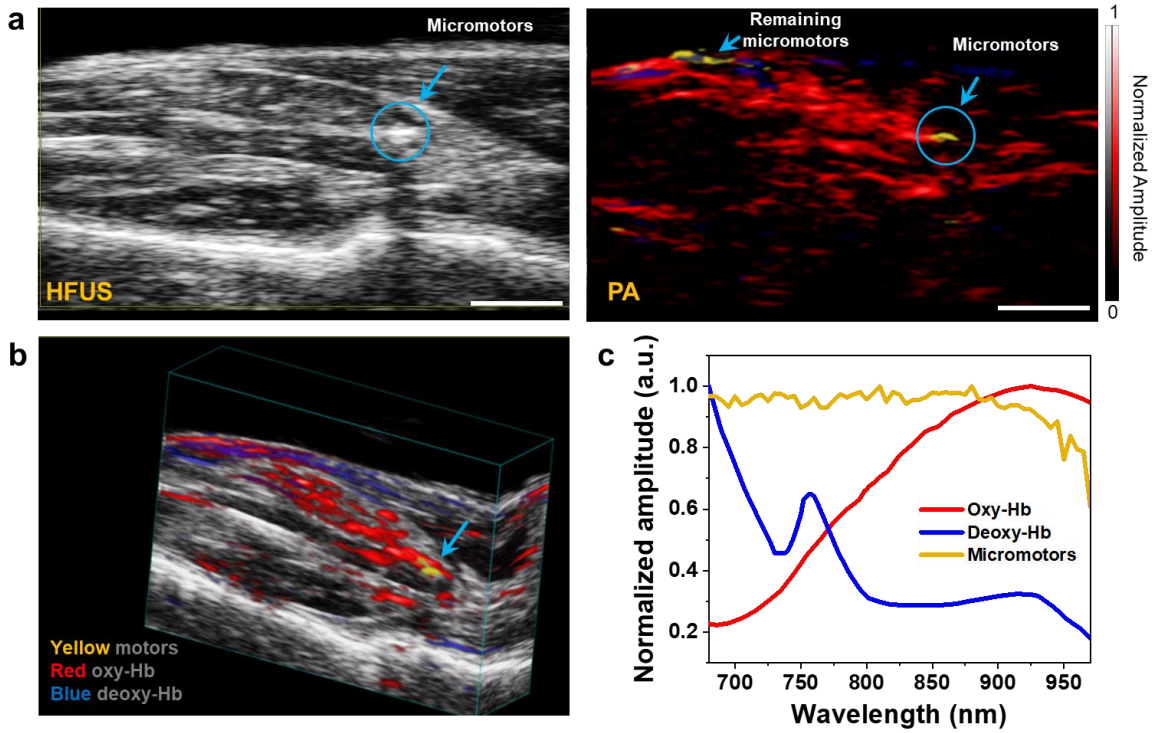

Figure S7. 3D multiplexing in vivo; a) Injection of micromotors into the mouse hind limb (popliteal lymph node fat pad) and HFUS and PA imaging of a swarm of micromotors (Yellow spot in PA mode shows the position of injected micromotors within tissue). The remaining micromotors from the syringe tip were also visible on the tissue top surface after taking it out. Scale bar: 2 mm. b) 3D reconstruction and spectral unmixing of the injected micromotors in tissue. c) PA signal strength of the injected micromotors (yellow), oxy (red), and deoxygenated (blue) hemoglobin.

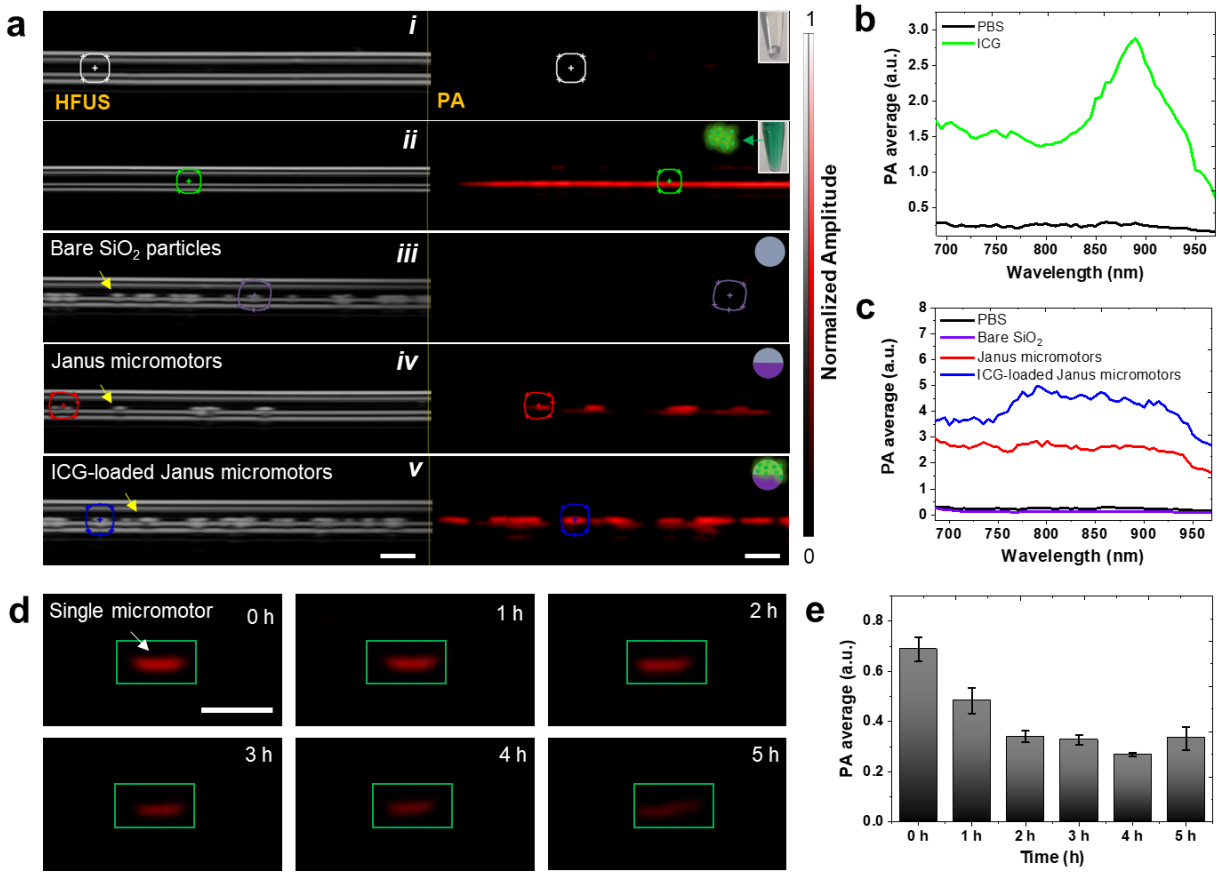

Figure S8. Preliminary study of ICG-loaded micromotors; a) HFUS and PA images of control (PBS) (i), ICG (ii), bare SiO_2 particles (iii), magnetic micromotors (iv), and ICG-labelled micromotors (v). Scale bar: 1 mm. b) PA spectral signal showing a distinct absorption peak at around 880 nm (green curve) of ICG when compared to the signal obtained from PBS. c) PA absorption spectrum of PBS, bare SiO_2, magnetic micromotor, and ICG-loaded micromotors. A comparable ROI was measured in each scenario where a single or few static micromotors were located. d) ICG- loaded single micromotors were monitored over 5 h to observe the release of ICG over time. Scale bar: 1 mm. e) PA signal intensity showing the decrease of ICG signal over 5 h.

Table S1. Imaging parameters for Hybrid HFUS and PA system implemented in this study.

Hybrid HFUS and PA system			
Static imaging		**Dynamic imaging**	
Wavelength (nm)	680-970 nm	Wavelength (nm)	800 nm
Frequency (MHz)	21 MHz	Frequency (MHz)	21 MHz
Detector elements	256	Detector elements	256
Axial resolution	75 µm	Axial resolution	75 µm
NA		Temporal resolution	US (max.320 fps) / PA (5-20 fps)
Penetration depth	~1 cm (ex vivo) ~2 cm (in vivo)	Penetration depth	~2 cm (in mice bladder and uterus)